DOI: 10.3901/CJME.2014.0930.156, available online at www.springerlink.com; www.cjmenet.com; www.cjmenet.com.cn

Compliance Analysis of a 3-DOF Spindle Head by Considering Gravitational Effects

LI Qi[1], WANG Manxin[1], HUANG Tian[1,*], and CHETWYND G Derek[2]

1 *Key Lab of Mechanism Theory and Equipment Design of Ministry of Education, Tianjin University 300074 China*
2 *School of Engineering, University of Warwick, Coventry CV4 7AL, UK*

Received March 31, 2014; revised September 22, 2014; accepted September 30, 2014

Abstract: The compliance modeling is one of the most significant issues in the stage of preliminary design for parallel kinematic machine(PKM). The gravity ignored in traditional compliance analysis has a significant effect on pose accuracy of tool center point(TCP) when a PKM is horizontally placed. By taking gravity into account, this paper presents a semi-analytical approach for compliance analysis of a 3-DOF spindle head named the A3 head. The architecture behind the A3 head is a 3-RPS parallel mechanism having one translational and two rotational movement capabilities, which can be employed to form the main body of a 5-DOF hybrid kinematic machine especially designed for high-speed machining of large aircraft components. The force analysis is carried out by considering both the externally applied wrench imposed upon the platform as well as gravity of all moving components. Then, the deflection analysis is investigated to establish the relationship between the deflection twist and compliances of all joints and links using semi-analytical method. The merits of this approach lie in that platform deflection twist throughout the entire task workspace can be evaluated in a very efficient manner. The effectiveness of the proposed approach is verified by the FEA and experiment at different configurations and the results show that the discrepancy of the compliances is less than 0.04 μm/N^{-1} and that of the deformations is less than 10μm. The computational and experimental results show that the deflection twist induced by gravity forces of the moving components has significant bearings on pose accuracy of the platform, providing an informative guidance for the improvement of the current design. The proposed approach can be easily applied to the compliance analysis of PKM by considering gravitational effects and to evaluate the deformation caused by gravity throughout the entire workspace.

Keywords: compliance modeling, gravity, spindle head

1 Introduction

High-speed machining of extra large aluminum aircraft parts with complex geometries(e.g. C-frame, wing rib, bow, spar, etc) is a challenging issue to the machine tool industry. The new demand would require a huge gantry 5-axis machine tool with tons of weight and large footprint in a traditional way. One promising solution to solve the problem is the use of a multiple-axis high-speed machining unit, composed of a 3-DOF PKM(parallel kinematic machines) spindle head plus the *x-y* movement capabilities[1]. This idea has already been demonstrated by very successful applications of ECOSPEED and ECOLINEAR[2] equipped with the Sprint Z3 Head[3–4] as a core component.

Stiffness is one of the most important indicators in performance evaluation of the spindle head as it is designed for high-speed machining where high rigidity and high accuracy are crucially required. These requirements lead to enthusiastic and extensive investigations into stiffness modeling, evaluation and optimization.

The approaches for the stiffness modeling can roughly be classified into two groups: 1) the numerical approach by means of finite element analysis(FEA)[5–7] or matrix structural analysis(MSA)[8–10], and 2) analytical or semi-analytical approach based upon the fundamental of robotics and the technology of FEA or structure mechanics. Although the FEA is the most precise method, it requires high computational cost as the models have to be re-meshed repeatedly with the changing configuration. Thus the FEA is more suitable at the final stage for the verification. For this reason, it is expected that a semi-analytical model can be developed that allows stiffness evaluation to be made throughout the entire workspace in an effective manner either in the preliminary or in the final design.

The early effort for analytical/semi-analytical stiffness modeling of parallel mechanisms can be traced back to the work[11] where the actuated joint stiffness was merely taken into account. By simultaneously accounting for component stiffness in terms of tensile/compression, bending and torsion, more extensive and comprehensive work is carried

* Corresponding author. E-mail: tianhuang@tju.edu.cn
Supported by National Natural Science Foundation of China(Grant No. 51135008), and PhD Programs Foundation of Ministry of Education of China (Grant No. 20110032130006)

out by ZHANG and GOSSELIN[12–14] in dealing with a stiffness analysis of the Tricept robots using an elegant concept of the "virtual joint" to formulate the bending compliance of a properly constrained passive limb, resulting in a simplified bending stiffness model represented by three lumped springs. Recently, the concept of "virtual joint" is significantly improved by PASHKEVICH, et al[15–18], resulting in a multidimensional lumped-parameter model formulated by the localized 6-DOF virtual springs to describe the link/joint compliances. Along this track, intensive and exhaustive investigations have been carried out in dealing with stiffness modeling of a variety of parallel mechanisms having different architectures[19–25]. Furthermore, the research interests have been placed to the technique of how to formulate the virtual joints precisely and effectively using FEA. i.e., the interface stiffness matrix of the components and the machine frame with complex geometry are evaluated by WANG, et al[26], using a commercialized FEA software. KLIMCHIK, et al[27], obtained the stiffness matrix of all the components by virtual experiment in FEA environment which was able to take into account the real shape of the joints and provided high accuracy. It should be pointed out that in the previous work dealing with analytical/semi-analytical stiffness modeling of parallel mechanisms, little attention has been paid to the deflections induced by gravity though they are no longer negligible especially when a device is horizontally placed in use. ZHAO, et al[28], and QUENNOUELLE, et al[29–30], extended the stiffness model by considering gravity as a lumped force. This treatment, however, is only valid when the components are assumed to be rigid, remaining an open issue to be investigated.

Based upon our previous work[31], this paper presents a semi-analytical compliance modeling approach of the A3 head by taking simultaneously into account for all significant joint/link compliances and the gravity of all movable components. Having consolidated by FEA and experiment at typical configurations, TCP deflections induced by gravity are evaluated throughout the entire workspace and the influence of each individual component gravity on the TCP deflections is investigated. The purpose of this investigation is to provide an informative guidance for the further improvement of the current design.

2 System Description and Inverse Position Analysis

Fig. 1 shows a CAD model of the A3 head. The topological architecture behind the A3 head is a 3-RPS parallel mechanism, which consists of a platform, a base and three identical RPS limbs. Here, R and S respectively represent a revolute and a spherical joints and the underlined P denotes an actuated prismatic joint. Driven by the actuated prismatic joints, the platform can achieve one translational and two rotational movement capabilities. For the detailed information of the A3 head, refer to Ref. [31].

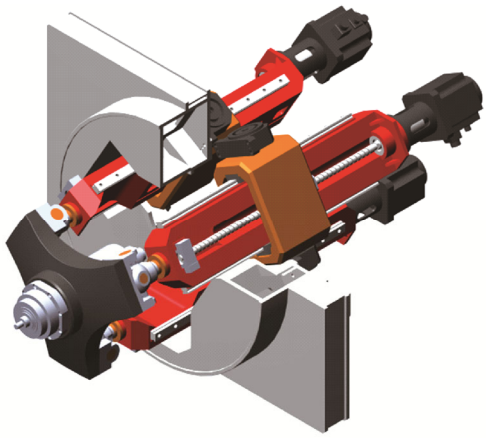

Fig. 1.　CAD model of the A3 head

Fig. 2 shows the schematic diagram of the A3 head. Let B_i be the centre of R joint connecting the ith limb with the base and A_i be that of the spherical joint connecting the limb with the platform. Thus, two equilateral triangles $\Delta B_1B_2B_3$ and $\Delta A_1A_2A_3$ can be formed. Then, we set the reference frame $\{R\}$ attached to the base such that $z \perp \Delta B_1B_2B_3$ and $y \perp \overline{B_2B_3}$ with its origin O being the intersection of three lines normal to the axes of the R joints. The same convention is adopted for the body fixed frame $\{R'\}$ attached to the platform with O' being the origin. For convenience in the definition of the component compliances within a limb, we place a set of limb reference frames $\{R_{j,i}\}$ attached to one of two elements of the jth joint in the ith limb with $\boldsymbol{s}_{j,i}$ being the unit vector of the joint axis. For this particular problem, $\{R_{1,i}\}$ is attached to base with the $z_{1,i}$ axis having the same direction to the z axis and the $x_{1,i}$ axis coincident with the axis of the R joint. $\{R_{2,i}\}$ is attached to the shaft of the R joint with the $x_{2,i}$ axis coincident with the $x_{1,i}$ and the $z_{2,i}$ axis coincident with the axis of the prismatic joint; $\{R_{1,i}\}$ and $\{R_{2,i}\}$ share the same origin B_i. In addition, $\{R_{j,i}\}$ (j=3–5) are attached to three parts of the spherical joint with A_i being the origins and $z_{3,i}(z_{2,i})$, $y_{4,i}(y_{3,i})$, $x_{5,i}(x_{4,i})$ being the joint axes as shown in Fig. 3.

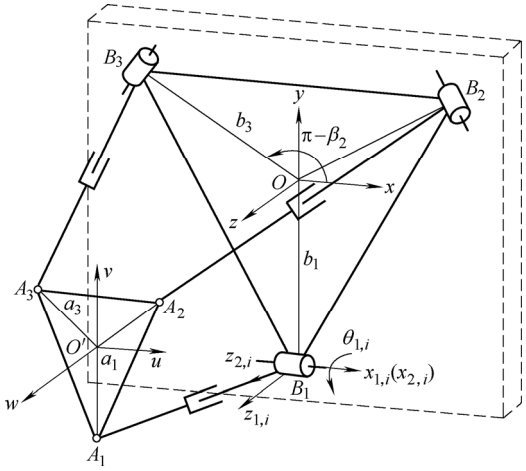

Fig. 2.　Schematic diagram of the A3 head

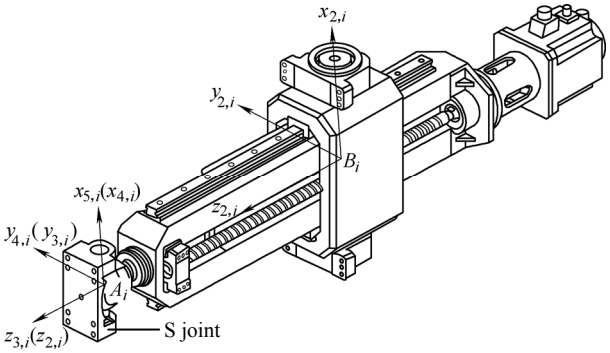

Fig. 3. Schematic diagram of body fixed frames of the S joint

As shown in Fig. 2, the position vector of the point O', $\boldsymbol{r}=(x \quad y \quad z)^{\mathrm{T}}$, can be expressed by

$$\boldsymbol{r}=\boldsymbol{b}_i+q_i\boldsymbol{s}_{2,i}-\boldsymbol{a}_i,\ i=1,2,3, \tag{1}$$

where q_i is the length of the ith limb, $\boldsymbol{b}_i$ and $\boldsymbol{a}_i$ are the position vectors pointing from O to B_i, and from O' to A_i, respectively. And

$$\boldsymbol{b}_i=b_i(\cos\beta_i \quad \sin\beta_i \quad 0)^{\mathrm{T}},\ \boldsymbol{a}_i=\boldsymbol{R}\boldsymbol{a}_{0i},$$
$$\boldsymbol{a}_{0i}=a_i(\cos\beta_i \quad \sin\beta_i \quad 0)^{\mathrm{T}},\ \beta_i=2\pi(i-1)/3-\pi/2,$$

where $\boldsymbol{R}$ is the orientation matrix of $\{R'\}$ with respect to $\{R\}$, and it can be formulated using three Euler's angles, i.e. the procession angle ψ, the nutation angle θ, and the spinning angle ϕ. Then, given a set of ψ, θ and z, the inverse position problem can be solved:

$$q_i=|\boldsymbol{r}-\boldsymbol{b}_i+\boldsymbol{a}_i|,\ \boldsymbol{s}_{2,i}=\boldsymbol{s}_{3,i}=(\boldsymbol{r}-\boldsymbol{b}_i+\boldsymbol{a}_i)/q_i, \tag{2}$$

$$\begin{aligned} x&=\frac{1}{2}a\sin 2\psi(1-\cos\theta),\\ y&=\frac{1}{2}a\cos 2\psi(1-\cos\theta),\\ \phi&=-\psi. \end{aligned} \tag{3}$$

Utilizing the method available in Ref. [31], the angles of the revolute and spherical joints can also be determined.

3 Compliance Analysis

This section formulates a semi-analytical compliance model of the A3 head that accounts simultaneously for all significant component compliance and the deflections induced by gravity of all movable components. For convenience, the moving platform and base are treated as rigid bodies by assuming that their rigidities are much higher than other components within the system.

3.1 Force analysis

Force analysis of the A3 head is concerned with the formulation of a linear map between the externally applied wrench and the reaction forces at the spherical joints as shown in Fig. 4. By taking moment of all force about O', the static equilibrium equations of the platform can be formulated by

$$\begin{pmatrix}\boldsymbol{f}\\ \boldsymbol{c}\end{pmatrix}=\sum_{i=1}^{3}f_{x_2,i}^{A}\begin{pmatrix}\boldsymbol{s}_{1,i}\\ \boldsymbol{a}_i\times\boldsymbol{s}_{1,i}\end{pmatrix}+\sum_{i=1}^{3}f_{y_2,i}^{A}\begin{pmatrix}\boldsymbol{n}_i\\ \boldsymbol{a}_i\times\boldsymbol{n}_i\end{pmatrix}+\sum_{i=1}^{3}f_{z_2,i}^{A}\begin{pmatrix}\boldsymbol{s}_{2,i}\\ \boldsymbol{a}_i\times\boldsymbol{s}_{2,i}\end{pmatrix}, \tag{4}$$

where $\boldsymbol{f}$ and $\boldsymbol{c}$ are the externally applied force and moment(including the cutting force and the gravitational force of the platform) imposed upon at O'; $\boldsymbol{n}_i=\boldsymbol{s}_{2,i}\times\boldsymbol{s}_{1,i}$; $f_{x_2,i}^{A}$, $f_{y_2,i}^{A}$ and $f_{z_2,i}^{A}$ are the reaction forces at A_i along the $x_{2,i}$, $y_{2,i}$ and $z_{2,i}$ axes, respectively. In order to solve $f_{y_2,i}^{A}$, draw free-body diagram of the ith limb-body assembly as shown in Fig. 5 and take moment of all forces about B_i. These implementations give

$$\begin{aligned}&\left((q_i-l_{\mathrm{L}})\boldsymbol{s}_{2,i}-l'_{\mathrm{L}}\boldsymbol{n}_i\right)\times(-m_{\mathrm{L}}g\hat{\boldsymbol{y}})+q_i\boldsymbol{s}_{2,i}\times\\ &\left(f_{x_2,i}^{A}\boldsymbol{s}_{1,i}+f_{y_2,i}^{A}\boldsymbol{n}_i\right)+\tau_{y_2,i}^{B}\boldsymbol{n}_i=0,\end{aligned} \tag{5}$$

where $\tau_{y_2,i}^{B}$ represents the reaction couple about the axis, m_{L} is the mass of limb body assembly, and l_{L} (l'_{L}) is the projection of the distance from mass center C_{L} of limb-body assembly to A_i along $\boldsymbol{s}_{2,i}$ ($\boldsymbol{n}_i$), Note that the so-called limb-body assembly here is exclusive of the part of the spherical joint rigidly connecting with the platform and the block of the R joint connecting the limb body via the prismatic joint. $\hat{\boldsymbol{y}}$ is the unit vector placed in the direction opposite to the gravity field.

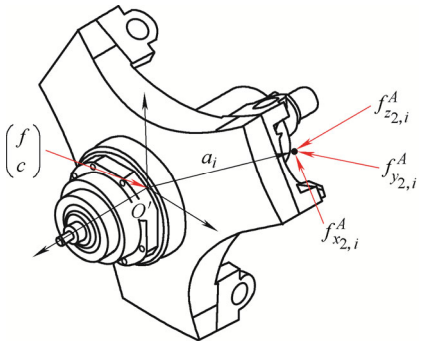

Fig. 4. Free-body diagram of the platform

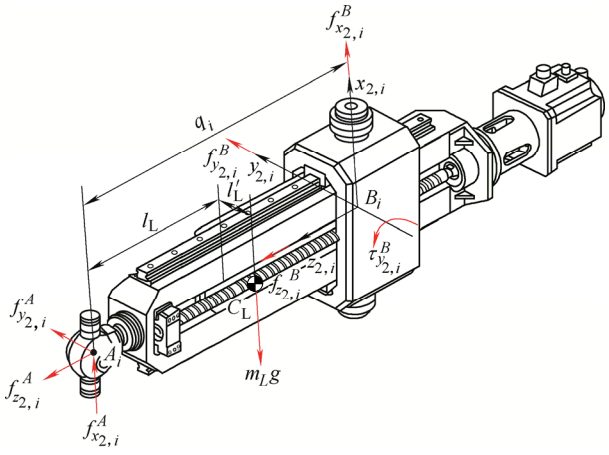

Fig. 5. Free-body diagram of the ith limb-body assembly

Then, taking dot product on both side of Eq. (5) with $\boldsymbol{s}_{1,i}$ leads to

$$f^A_{y_2,i}=\frac{m_{\mathrm{L}}g}{q_i}\left[(q_i-l_{\mathrm{L}})\boldsymbol{n}_i^{\mathrm{T}}+l'_{\mathrm{L}}\boldsymbol{s}_{2,i}^{\mathrm{T}}\right]\hat{\boldsymbol{y}},\ i=1,2,3. \tag{6}$$

Substituting Eq. (6) into Eq. (4) and rewriting in matrix form, results in

$$\$_{\mathrm{w}}=\boldsymbol{J}^{\mathrm{T}}\boldsymbol{\rho}_{\mathrm{w}}, \tag{7}$$

$$\$_{\mathrm{w}}=\begin{pmatrix}\boldsymbol{f}\\ \boldsymbol{c}\end{pmatrix}+\$'_{\mathrm{w}},$$

$$\$'_{\mathrm{w}}=-\sum_{i=1}^{3}\frac{m_{\mathrm{L}}g}{q_i}\left[(q_i-l_{\mathrm{L}})\boldsymbol{n}_i^{\mathrm{T}}+l'_{\mathrm{L}}\boldsymbol{s}_{2,i}^{\mathrm{T}}\right]\hat{\boldsymbol{y}}\begin{pmatrix}\boldsymbol{n}_i\\ \boldsymbol{a}_i\times\boldsymbol{n}_i\end{pmatrix},$$

$$\boldsymbol{J}=\begin{pmatrix}\boldsymbol{J}_{\mathrm{a}}^{\mathrm{T}} & \boldsymbol{J}_{\mathrm{c}}^{\mathrm{T}}\end{pmatrix}^{\mathrm{T}},\ \boldsymbol{\rho}_{\mathrm{w}}=\begin{pmatrix}\boldsymbol{\rho}_{\mathrm{wa}}^{\mathrm{T}} & \boldsymbol{\rho}_{\mathrm{wc}}^{\mathrm{T}}\end{pmatrix}^{\mathrm{T}},$$

$$\boldsymbol{J}_{\mathrm{a}}=\begin{pmatrix}\hat{\$}_{\mathrm{wa},1} & \hat{\$}_{\mathrm{wa},2} & \hat{\$}_{\mathrm{wa},3}\end{pmatrix}^{\mathrm{T}},\ \hat{\$}_{\mathrm{wa},i}=\begin{pmatrix}\boldsymbol{s}_{2,i}\\ \boldsymbol{a}_i\times\boldsymbol{s}_{2,i}\end{pmatrix},$$

$$\boldsymbol{J}_{\mathrm{c}}=\begin{pmatrix}\hat{\$}_{\mathrm{wc},1} & \hat{\$}_{\mathrm{wc},2} & \hat{\$}_{\mathrm{wc},3}\end{pmatrix}^{\mathrm{T}},\ \hat{\$}_{\mathrm{wc},i}=\begin{pmatrix}\boldsymbol{s}_{1,i}\\ \boldsymbol{a}_i\times\boldsymbol{s}_{1,i}\end{pmatrix},$$

$$\boldsymbol{\rho}_{\mathrm{wa}}=\begin{pmatrix}\rho_{\mathrm{wa},1} & \rho_{\mathrm{wa},2} & \rho_{\mathrm{wa},3}\end{pmatrix}^{\mathrm{T}},\ \rho_{\mathrm{wa},i}=f^A_{z_2,i},$$

$$\boldsymbol{\rho}_{\mathrm{wc}}=\begin{pmatrix}\rho_{\mathrm{wc},1} & \rho_{\mathrm{wc},2} & \rho_{\mathrm{wc},3}\end{pmatrix}^{\mathrm{T}},\ \rho_{\mathrm{wc},i}=f^A_{x_2,i},$$

where $\$_{\mathrm{w}}$ represents resultant of externally applied wrench imposed at O', including the contributions from cutting force, gravity of the platform itself and that of the limb-body assemblies transmitted through the spherical joints to the platform. $\boldsymbol{J}$ is the overall Jacobian with $\boldsymbol{J}_{\mathrm{a}}$ ($\boldsymbol{J}_{\mathrm{c}}$) being the Jacobian of actuations(constraints), and its element $\hat{\$}_{\mathrm{wa},i}$($\hat{\$}_{\mathrm{wc},i}$) represents the unit wrench of actuations(constraints) imposed by the ith limb to the platform. $\boldsymbol{\rho}_{\mathrm{w}}$ is the joint force vector with $\boldsymbol{\rho}_{\mathrm{wa}}$ ($\boldsymbol{\rho}_{\mathrm{wc}}$) being the components corresponding to $\boldsymbol{J}_{\mathrm{a}}$ ($\boldsymbol{J}_{\mathrm{c}}$), and its element $\rho_{\mathrm{wa},i}$ ($\rho_{\mathrm{wc},i}$) can be understood as the magnitude of $\hat{\$}_{\mathrm{wa},i}$ ($\hat{\$}_{\mathrm{wc},i}$). Thus, the physical meaning of Eq. (7) can be interpreted as the externally applied wrench must be equilibrated by all wrenches of actuations and constraints imposed by all limbs to the platform.

3.2 Deflection analysis

The purpose of deflection analysis of the A3 head is to formulate the linear map between deflection twist of the platform at O' and the linear deflections at A_i due to the components compliances within limbs. Thus, a simple first-order perturbation gives

$$\delta\boldsymbol{r}+\delta\boldsymbol{\alpha}\times\boldsymbol{a}_i=\delta^A_{x_2,i}\boldsymbol{s}_{1,i}+\delta^A_{y_2,i}\boldsymbol{n}_i+\delta^A_{z_2,i}\boldsymbol{s}_{2,i},\ i=1,2,3, \tag{8}$$

where $\delta\boldsymbol{r}$ and $\delta\boldsymbol{\alpha}$ are the linear deflection at O' and the angular deflection of the platform, $\delta^A_{x_2,i}$ and $\delta^A_{z_2,i}$ represent respectively the bending deflection along $x_{2,i}$ axis and extension/compression deflection along $z_{2,i}$ axis at A_i due to the limb component compliance. Whilst $\delta^A_{y_2,i}$ is the linear rigid-body displacement at A_i along $y_{2,i}$ axis such that the compatibility can be satisfied because all limbs share the same platform. Then, taking dot production on both side of Eq. (8) with $\boldsymbol{s}_{2,i}$ and $\boldsymbol{s}_{1,i}$, and rewriting in matrix form, yields

$$\$_{\mathrm{t}}=\boldsymbol{G}\boldsymbol{\rho}_{\mathrm{t}}, \tag{9}$$

$$\$_{\mathrm{t}}=\begin{pmatrix}\delta\boldsymbol{r}^{\mathrm{T}} & \delta\boldsymbol{\alpha}^{\mathrm{T}}\end{pmatrix}^{\mathrm{T}},\ \boldsymbol{G}=\boldsymbol{J}^{-1}=\begin{pmatrix}\boldsymbol{G}_{\mathrm{a}} & \boldsymbol{G}_{\mathrm{c}}\end{pmatrix},$$

$$\boldsymbol{\rho}_{\mathrm{t}}=\begin{pmatrix}\boldsymbol{\rho}_{\mathrm{ta}}^{\mathrm{T}} & \boldsymbol{\rho}_{\mathrm{tc}}^{\mathrm{T}}\end{pmatrix}^{\mathrm{T}},\ \boldsymbol{\rho}_{\mathrm{ta}}=\begin{pmatrix}\rho_{\mathrm{ta},1} & \rho_{\mathrm{ta},2} & \rho_{\mathrm{ta},3}\end{pmatrix}^{\mathrm{T}},\ \rho_{\mathrm{ta},i}=\delta^A_{z_2,i},$$

$$\boldsymbol{\rho}_{\mathrm{tc}}=\boldsymbol{\rho}'_{\mathrm{tc}}+\boldsymbol{\rho}''_{\mathrm{tc}},$$

$$\boldsymbol{\rho}'_{\mathrm{tc}}=\begin{pmatrix}\rho'_{\mathrm{tc},1} & \rho'_{\mathrm{tc},2} & \rho'_{\mathrm{tc},3}\end{pmatrix}^{\mathrm{T}},\ \rho'_{\mathrm{tc},i}=\delta'^A_{x_2,i},$$

$$\boldsymbol{\rho}''_{\mathrm{tc}}=\begin{pmatrix}\rho''_{\mathrm{tc},1} & \rho''_{\mathrm{tc},2} & \rho''_{\mathrm{tc},3}\end{pmatrix}^{\mathrm{T}},\ \rho''_{\mathrm{tc},i}=\delta''^A_{x_2,i},$$

where $\$_{\mathrm{t}}$ represents the deflection twist of the platform at O', $\boldsymbol{\rho}_{\mathrm{t}}$ is the joint deflection vector with $\boldsymbol{\rho}_{\mathrm{ta}}$ ($\boldsymbol{\rho}_{\mathrm{tc}}$) being those associated with $\boldsymbol{G}_{\mathrm{a}}$ ($\boldsymbol{G}_{\mathrm{c}}$). It should be noted that the element $\rho_{\mathrm{tc},i}$ in $\boldsymbol{\rho}_{\mathrm{tc}}$ contains two components, i.e. $\rho'_{\mathrm{tc},i}$ caused by $\rho_{\mathrm{wc},i}$ due to the compliance of the limb and $\rho''_{\mathrm{tc},i}$ caused by the distributed gravitational force of the limb itself due to its compliance. Further discussion will be made in Section 3.5 for the formulation of $\rho''_{\mathrm{tc},i}$.

3.3 Compliance modeling

Having developed the force and deflection models at hand, little more effort is required to formulate the compliance model of the A3 head by taking into account the effect of gravitational forces in an unloaded equilibrium configuration. Assuming each component is linearly elastic, Hooke's law gives

$$\boldsymbol{\rho}_{\mathrm{ta}}=\bar{\boldsymbol{C}}_{\mathrm{a}}\boldsymbol{\rho}_{\mathrm{wa}},\ \boldsymbol{\rho}_{\mathrm{tc}}=\bar{\boldsymbol{C}}_{\mathrm{c}}\boldsymbol{\rho}_{\mathrm{wc}}, \tag{10}$$

$$\bar{\boldsymbol{C}}_{\mathrm{a}}=\begin{pmatrix}c_{\mathrm{a},1} & & \\ & c_{\mathrm{a},2} & \\ & & c_{\mathrm{a},3}\end{pmatrix},\ \bar{\boldsymbol{C}}_{\mathrm{c}}=\begin{pmatrix}c_{\mathrm{c},1} & & \\ & c_{\mathrm{c},2} & \\ & & c_{\mathrm{c},3}\end{pmatrix},$$

where $\bar{\boldsymbol{C}}_{\mathrm{a}}$ ($\bar{\boldsymbol{C}}_{\mathrm{c}}$) is referred to as the component compliance matrix of actuations(constraints). Its elements, $c_{\mathrm{a},i}$ ($c_{\mathrm{c},i}$) can be interpreted physically as the deflection along $z_{2,i}$ ($x_{2,i}$) axis caused by unit joint force $\rho_{\mathrm{wa},i}$ ($\rho_{\mathrm{wc},i}$) at A_i, Note that $c_{\mathrm{a},i}$ and $c_{\mathrm{c},i}$ are usually not constants but configuration dependent. Substituting Eq. (7) and Eq. (10) into Eq. (9) and assuming the system is in a non-singular configuration finally results in the compliance model of the A3 head when gravitational effects are considered

$$\$_{\mathrm{t}}=\boldsymbol{C}\$_{\mathrm{w}}+\boldsymbol{G}_{\mathrm{c}}\boldsymbol{\rho}''_{\mathrm{tc}}, \tag{11}$$

where $\boldsymbol{C}=\boldsymbol{C}_{\mathrm{a}}+\boldsymbol{C}_{\mathrm{c}}$, $\boldsymbol{C}_{\mathrm{a}}=\boldsymbol{G}_{\mathrm{a}}\bar{\boldsymbol{C}}_{\mathrm{a}}\boldsymbol{G}_{\mathrm{a}}^{\mathrm{T}}$, $\boldsymbol{C}_{\mathrm{c}}=\boldsymbol{G}_{\mathrm{c}}\bar{\boldsymbol{C}}_{\mathrm{c}}\boldsymbol{G}_{\mathrm{c}}^{\mathrm{T}}$.

3.4 Formulation of $\bar{\boldsymbol{C}}_{\mathrm{a}}$ and $\bar{\boldsymbol{C}}_{\mathrm{c}}$

In order to formulate $\bar{\boldsymbol{C}}_{\mathrm{a}}$ and $\bar{\boldsymbol{C}}_{\mathrm{c}}$, we omit the limb

identifier for the time being. We assume that the compliance matrix of a component/joint evaluated in the local frame $\{R_j\}$ with respect to the point D can approximately be formulated as

$$\boldsymbol{C}_j^D=\begin{pmatrix}\boldsymbol{C}_{j,t}^D & \\ & \boldsymbol{C}_{j,r}^D\end{pmatrix},\ \boldsymbol{C}_{j,t}^D=\begin{pmatrix}c_{x_j}^D & & \\ & c_{y_j}^D & \\ & & c_{z_j}^D\end{pmatrix},\ \boldsymbol{C}_{j,r}^D=\begin{pmatrix}c_{\alpha_j}^D & & \\ & c_{\beta_j}^D & \\ & & c_{\gamma_j}^D\end{pmatrix}, \tag{12}$$

where $\boldsymbol{C}_{j,t}^D(\boldsymbol{C}_{j,r}^D)$ denotes the linear(angular) compliance matrices with respect to D with its diagonal elements $c_{x_j}^D$, $c_{y_j}^D$, $c_{z_j}^D$ ($c_{\alpha_j}^D$, $c_{\beta_j}^D$, $c_{\gamma_j}^D$) being the linear(angular) compliance coefficients along(about) the x_j, y_j, z_j axes. Note that all elements in $\bar{\boldsymbol{C}}_a$ and $\bar{\boldsymbol{C}}_c$ are evaluated in $\{R_2\}$ with respect to A and thereby the matrix is of the form

$$\boldsymbol{C}_2^A=\begin{pmatrix}c_{x_2}^A & & \\ & \infty & \\ & & c_{z_2}^A\end{pmatrix}. \tag{13}$$

Then the relationship between $\boldsymbol{C}_j^D$ and $\boldsymbol{C}_2^A$ can be formulated by the principle of virtual work

$$\boldsymbol{C}_2^A=\boldsymbol{R}_{j2}\boldsymbol{C}_{j,t}^D\boldsymbol{R}_{j2}^{\mathrm{T}}-\tilde{\boldsymbol{p}}\boldsymbol{R}_{j2}\boldsymbol{C}_{j,r}^D\boldsymbol{R}_{j2}^{\mathrm{T}}\tilde{\boldsymbol{p}}, \tag{14}$$

where $\boldsymbol{R}_{j2}=\begin{pmatrix}\boldsymbol{u}_{j2} & \boldsymbol{v}_{j2} & \boldsymbol{w}_{j2}\end{pmatrix}$ denotes the orientation matrix of $\{R_j\}$ with respect to $\{R_2\}$, and $\tilde{\boldsymbol{p}}$ is the skew matrix of the vector $\boldsymbol{p}$ pointing from A to D.

For convenience to evaluate the component compliances, we group all the parts of the RPS limb into four sub-assemblies as shown in Fig. 6 and Fig. 7, including the S joint, the limb body assembly(including the lead-screw and its supporting bearing), the P joint and the R joint. Consequently, the elements in $\bar{\boldsymbol{C}}_{\mathrm{a}}$ ($\bar{\boldsymbol{C}}_{\mathrm{c}}$) can be modeled by

$$\begin{aligned}c_{\mathrm{a}}&=c_{z_2,\mathrm{S\_joint}}^A+c_{z_2,\mathrm{L\_body}}^A+c_{z_2,\mathrm{P\_joint}}^A+c_{z_2,\mathrm{R\_joint}}^A,\\ c_{\mathrm{c}}&=c_{x_2,\mathrm{S\_joint}}^A+c_{x_2,\mathrm{L\_body}}^A+c_{x_2,\mathrm{P\_joint}}^A+c_{x_2,\mathrm{R\_joint}}^A,\end{aligned} \tag{15}$$

where $c_{z_2,\mathrm{S\_joint}}^A$, $c_{z_2,\mathrm{L\_body}}^A$, $c_{z_2,\mathrm{P\_joint}}^A$ and $c_{z_2,\mathrm{R\_joint}}^A$ ($c_{x_2,\mathrm{S\_joint}}^A$, $c_{x_2,\mathrm{L\_body}}^A$, $c_{x_2,\mathrm{P\_joint}}^A$ and $c_{x_2,\mathrm{R\_joint}}^A$) represent the extension/compression(bending) compliance coefficients of the S joint, the limb-body assembly, the P joint and the R joint at A along the z_2 (x_2) axis. Utilizing Eq. (15), these compliance coefficients can further be detailed as follows in order to closely related to the mechanical components:

$$\begin{aligned}c_{z_2,\mathrm{S\_joint}}^A&=\left(\sum_{j=3}^{5}c_{x_j,\mathrm{S\_joint}}^A\boldsymbol{u}_{j2}\boldsymbol{u}_{j2}^{\mathrm{T}}+c_{y_j,\mathrm{S\_joint}}^A\boldsymbol{v}_{j2}\boldsymbol{v}_{j2}^{\mathrm{T}}+c_{z_j,\mathrm{S\_joint}}^A\boldsymbol{w}_{j2}\boldsymbol{w}_{j2}^{\mathrm{T}}\right)(3,3),\\ c_{x_2,\mathrm{S\_joint}}^A&=\left(\sum_{j=3}^{5}c_{x_j,\mathrm{S\_joint}}^A\boldsymbol{u}_{j2}\boldsymbol{u}_{j2}^{\mathrm{T}}+c_{y_j,\mathrm{S\_joint}}^A\boldsymbol{v}_{j2}\boldsymbol{v}_{j2}^{\mathrm{T}}+c_{z_j,\mathrm{S\_joint}}^A\boldsymbol{w}_{j2}\boldsymbol{w}_{j2}^{\mathrm{T}}\right)(1,1),\end{aligned} \tag{16}$$

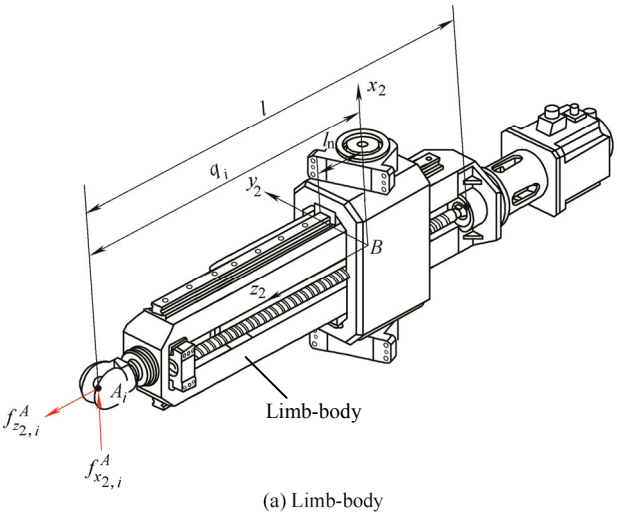

(a) Limb-body

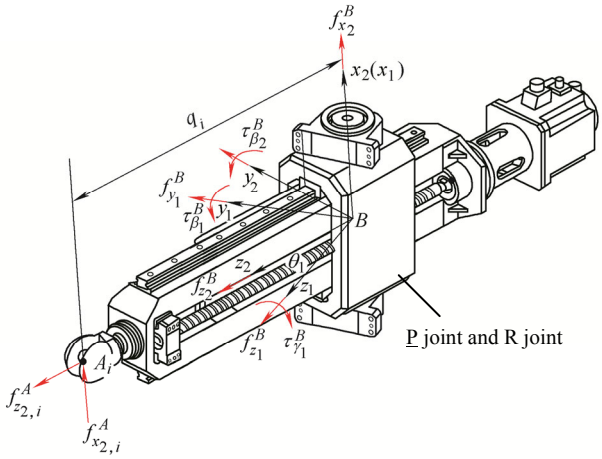

(b) Pjoint and R joint

Fig. 6. Free body diagram of RPS sub-assemblies

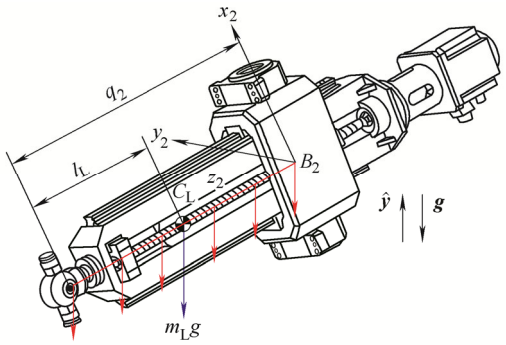

Fig. 7. Schematic of RPS limb-body under the gravitational field at θ=0°

$$\begin{aligned}c_{x_2,\mathrm{P\_joint}}^A&=c_{x_2,\mathrm{P\_joint}}^B+q^2c_{\beta_2,\mathrm{P\_joint}},\\ c_{z_2,\mathrm{P\_joint}}^A&=c_{z_2,\mathrm{bearing}}+c_{z_2,\mathrm{nut}}+c_{z_2,\mathrm{screw}},\\ c_{z_2,\mathrm{screw}}&=(l-l_{\mathrm{n}}-q)/EA,\end{aligned} \tag{17}$$

$$\begin{aligned}c_{x_2,\mathrm{R\_joint}}^A&=c_{x_2,\mathrm{R\_joint}}^B+q^2c_{\beta_2,\mathrm{R\_joint}},\\ c_{z_2,\mathrm{R\_joint}}^A&=c_{z_1,\mathrm{R\_joint}}^B\cos^2\theta_1+c_{y_1,\mathrm{R\_joint}}^B\sin^2\theta_1,\\ c_{\beta_2,\mathrm{R\_joint}}&=c_{\beta_1,\mathrm{R\_joint}}\cos^2\theta_1+c_{\gamma_1,\mathrm{R\_joint}}\sin^2\theta_1,\end{aligned} \tag{18}$$

where $c^A_{x_j,\text{S\_joint}}$, $c^A_{y_j,\text{S\_joint}}$ and $c^A_{z_j,\text{S\_joint}}$ are the linear compliance coefficients of the (j–2)th revolute joint within the spherical joint along the x_j, y_j, z_j (j=3–5) axes; $c^B_{x_2,\text{P\_joint}}$ ($c^B_{\beta_2,\text{P\_joint}}$) is the linear(angular) compliance coefficients of the P joint evaluated at B along the x_2 axis(about the y_2 axis); $c_{z_2,\text{bearing}}$, $c_{z_2,\text{nut}}$ and $c_{z_2,\text{screw}}$ are the compliance coefficients of rear support bearing, nut and lead-screw along the z_2 axis; EA is the tensile modulus of the lead-screw[31]. $c^B_{x_2,\text{R\_joint}}$ and $c^B_{z_2,\text{R\_joint}}$ ($c^B_{\beta_2,\text{R\_joint}}$) are the linear(angular) compliance coefficients of the R joint evaluated at B along the x_2 and z_2 axes(about the y_2 axis); $c_{\beta_1,\text{R\_joint}}$ and $c_{\gamma_1,\text{R\_joint}}$ ($c^B_{y_1,\text{R\_joint}}$ and $c^B_{z_1,\text{R\_joint}}$) are the angular(linear) compliance coefficients of the R joint about the y_1 and z_1 axis.

3.5 Formulation of $\boldsymbol{\rho}''_{tc}$

According to Eq. (11), $\rho''_{\text{tc},i}=\delta''^{A}_{x_2,i}$ denotes the elastic deflection caused by the distributed gravitational forces of the limb due to its compliance. For convenience, this deflection can be divided into two parts, i.e. $\delta''^{A}_{x_2,i,1}$ caused by the compliance of R joint and P joint under the action of the gravity of limb-body, $\delta''^{A}_{x_2,i,2}$ caused by the compliance of limb-body under the effect of its own gravitational field. These considerations lead to

$$\begin{aligned}\delta''^{A}_{x_2,i}&=\delta''^{A}_{x_2,i,1}+\delta''^{A}_{x_2,i,2},\\ \delta''^{A}_{x_2,i,1}&=m_{\text{L}}g\left(c^B_{x_2,i,\text{P\_joint}}+c^B_{x_2,i,\text{R\_joint}}+\right.\\ &\left.l_{\text{L}}\left(q_i-l_{\text{L}}\right)\left(c_{\beta_2,i,\text{P\_joint}}+c_{\beta_2,i,\text{R\_joint}}\right)\right)\boldsymbol{s}^{\text{T}}_{1,i}\hat{\boldsymbol{y}},\\ \delta''^{A}_{x_2,i,2}&=\delta^{A}_{x_2,i,\text{L\_body}}\boldsymbol{s}^{\text{T}}_{1,i}\hat{\boldsymbol{y}},\end{aligned}\tag{19}$$

where $\delta^A_{x_2,i,\text{L\_body}}$ denotes the linear deflection of the ith limb-body itself at A_i along the x_2 axis under the action of its own gravitational field when $\boldsymbol{s}^{\text{T}}_{1,i}\hat{\boldsymbol{y}}=1$, which can be formulated as a function of q_i by an interpolation technique using the data obtained from FEA.

4 Example

Now we take the A3 head shown in Fig. 1 as an example to investigate the TCP deflection caused by gravity. The dimensions and workspace of A3 head are given in Table 1. Tables 2–4 show the compliance coefficients of the S joint, P joint and R joint, all are evaluated by means of FEA and data from handbooks. The compliance coefficients of the nut, rear bearing and limb-body along the $z_{2,i}$ axis, and the tensile modulus EA of the lead-screw are given in Table 5. The masses and their locations of limb-body and platform are given in Table 6. Fig. 8 shows the bending compliance $c^A_{x_2,\text{L\_body}}$ of the limb-body at A_i along the $x_{2,i}$ axis and its linear deflection $\delta^A_{x_2,\text{L\_body}}$ due to the gravitational field versus q.

Table 1. Dimensions and workspace of A3

Parameter	Value
Radius of platform a/mm	250
Radius of base b/mm	250
Minimum distance between platform and base at origin configuration $d_{\min}$/ mm	540
Maximum stroke of A3 head $s_{\max}$/mm	200
Maximum nutation angle of platform $\theta_{\max}$/(°)	40

Table 2. Linear compliance coefficients of the components of S joint

Linear compliance coefficient /(nm • N^{-1})	Value
The 1st revolute joint along x_3 axis $c^A_{x_3,\text{S\_joint}}$	42.890
The 1st revolute joint along y_3 axis $c^A_{y_3,\text{S\_joint}}$	42.616
The 1st revolute joint along z_3 axis $c^A_{z_3,\text{S\_joint}}$	1.605
The 2nd revolute joint along x_4 axis $c^A_{x_4,\text{S\_joint}}$	8.921
The 2nd revolute joint along y_4 axis $c^A_{y_4,\text{S\_joint}}$	4.664
The 2nd revolute joint along z_4 axis $c^A_{z_4,\text{S\_joint}}$	9.965
The 3rd revolute joint along x_5 axis $c^A_{x_5,\text{S\_joint}}$	1.479
The 3rd revolute joint along y_5 axis $c^A_{y_5,\text{S\_joint}}$	2.241
The 3rd revolute joint along z_5 axis $c^A_{z_5,\text{S\_joint}}$	2.877

Table 3. Linear compliance coefficients of the components of P joint and R joint

Linear compliance coefficient /(nm • N^{-1})	Value
P joint at B along x_2 axis $c^B_{x_2,\text{P\_joint}}$	8.090 0
P joint at B along z_2 axis $c^B_{z_2,\text{P\_joint}}$	2.158 0
R joint at B along x_2 axis $c^B_{x_2,\text{R\_joint}}$	0.852 5
R joint at B along y_2 axis $c^B_{y_2,\text{R\_joint}}$	0.770 6
R joint at B along z_2 axis $c^B_{z_2,\text{R\_joint}}$	0.656 9

Table 4. Angular compliance coefficients of the components of P joint and R joint

Angular compliance coefficient /(rad • (GN • m)$^{-1}$)	Value
P joint at B about y_2 axis $c_{\beta_2,\text{P\_joint}}$	117.110
R joint at B about y_1 axis $c_{\beta_1,\text{R\_joint}}$	5.162
R joint at B about z_1 axis $c_{\gamma_1,\text{R\_joint}}$	7.295

Table 5. Parameters to determine the compliance coefficients of nut, rear bearing, limb-body and lead-screw

Parameter	Value
Compliance coefficient of nut $c_{\text{a,nut}}$/(nm • N^{-1})	3.289 5
Compliance coefficient of rear bearing $c_{\text{a,bearing}}$/(nm • N^{-1})	0.588 2
Compliance coefficient of limb-body $c_{\text{a,L\_body}}$/(nm • N^{-1})	2.416 5
Tensile modulus EA/MN	90.1
Length of limb-body l/mm	1105
Half length of P joint l_{n}/mm	125

Table 6. Masses and their locations of the platform and limb-body

Parameter	Value
Distance from C to O' l_C/mm	490
Distance from the gravity center of platform to O' l_g/mm	86.3
Distance from C_L to A_i l_L/mm	800
Distance from C_L to $z_{2,i}$ l'_L/mm	19
Mass of platform m_M/kg	148.56
Mass of limb-body m_L/kg	123.37

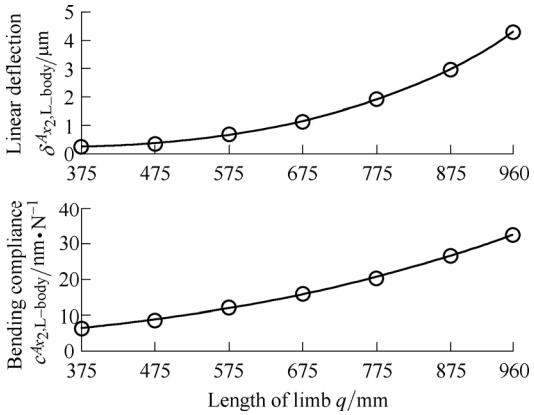

Fig. 8. Linear deflection $\delta^A_{x_2,\text{L\_body}}$ and bending compliance $c^A_{x_2,\text{L\_body}}$ of the limb-body assembly versus q

Then, the TCP deflection, $\$^C_{t,G}$ can be divided into three components:

$$\$^C_{t,G} = \$^m_t + \$'_t + \$''_t, \tag{20}$$

where $\$^m_t = \boldsymbol{T}_C \boldsymbol{C} \$^m_w$ is the deflection due to the gravity of the platform, and $\$'_t = \boldsymbol{T}_C \boldsymbol{C} \$'_w$ and $\$''_t = \boldsymbol{T}_C \boldsymbol{G}_c \boldsymbol{\rho}''_{tc}$ represent the deflections of TCP due to the gravity of limb-body assembly. $\boldsymbol{T}_C$ is the adjoint matrix of $\{R_C\}$ from O' to C as Fig. 9. And we denote $\$^C_{t,G}(i)$ (i=1–6) as the ith element of $\$^C_{t,G}$, i.e. δ_x, δ_y, δ_z, γ_x, γ_y and γ_z, sequentially representing the linear/angular deflection along/about the three orthogonal axes of the frame $\{R_C\}$.

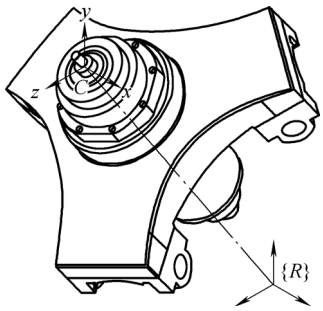

Fig. 9. Schematic of tool tip frame

4.1 Deflection analysis

Figs. 10(a)–(f) show the distributions of δ_x, δ_y, δ_z, γ_x, γ_y and γ_z in three layers(θ=0–40°, ψ=0–360°, z=540 mm, 640 mm, 740 mm) of workspace W_t due to gravitational field. It can be seen that δ_y, δ_z and γ_x are symmetrically distributed with respect to the y-z plane, while δ_x, γ_y and γ_z are anti-symmetric distributed with respect to that same plane. The distribution of $|\delta_y|$ increases with the increase of z, while others almost keep unchanged. $|\delta_y|$ is much higher than $|\delta_x|$ and $|\delta_z|$ in value, meaning that the deflection caused by gravitational field is mainly dominated by $|\delta_y|$ as predicted.

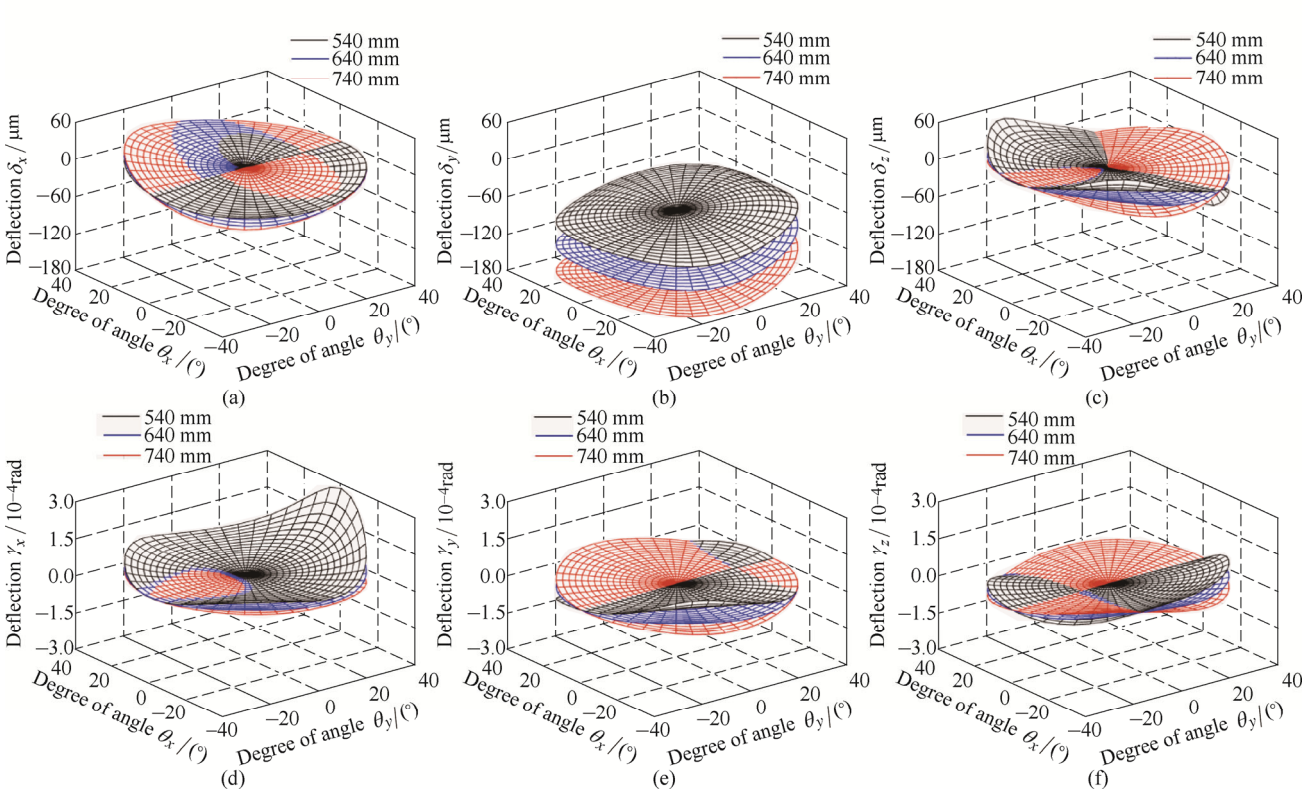

Fig. 10. Distributions of the deflection of TCP under the gravitational field: θ=0–40°, ψ=0–360°, z=540 mm, 640 mm, 740 mm

Figs. 11(a)–(c) shows the distributions of δ_y due to gravitational forces of the platform, the limb body assemblies transmitted to the platform and the compliances of the limbs under actions of the their own distributed gravitational forces, as marked by $\$_t^m(2)$, $\$_t'(2)$ and $\$_t''(2)$, respectively. Compared to $\$_t'(2)$ and $\$_t''(2)$, $\$_t^m(2)$ is much greater, meaning that a light weight design is required platform is too heavy in weight. It can also be observed that the deflections caused by gravity of the platform and limb-body are opposite to each other in direction, leading the deflections to be reduced to some extent. Meanwhile, the significant difference between the $\$_t'(2)$ and $\$_t''(2)$ also indicates that there remains room for optimization and mass of the limb-body.

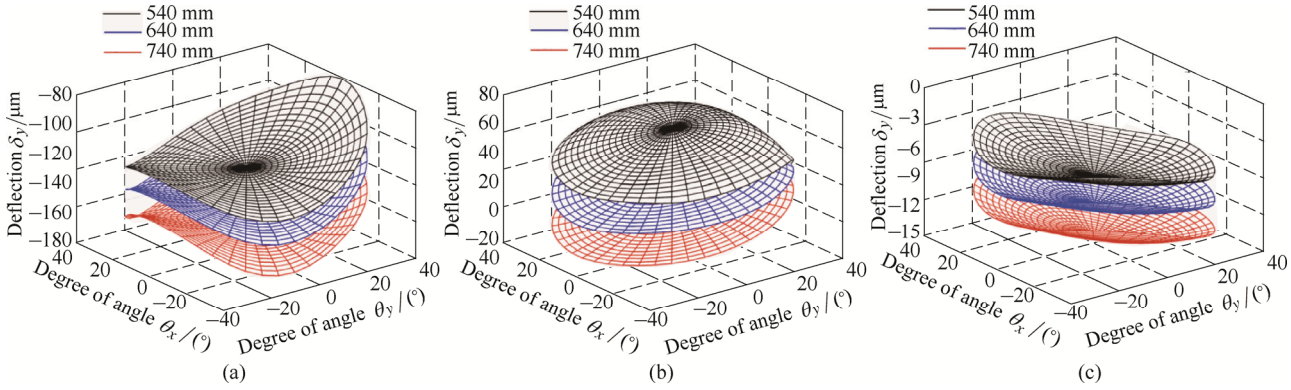

Fig. 11. Distributions of the deflection of TCP (a) $\$_t^m$; (b) $\$_t'$; (c) $\$_t''$ along y axis: θ=0–40°, ψ=0–360°, z=540 mm, 640 mm, 740 mm

4.2 FEA and experimental verification

In order to validate the semi-analytical model developed, FEA is carried out to verify δ_y obtained by the semi-analytical approach at four orientations(θ=0°; θ=40°, ψ=0°; θ=40°, ψ=90°; θ=40°, ψ=180°) in z=540 mm and z=740 mm. It can be seen from Table 7 and Figs. 12–13 that the results match very well.

Table 7. Comparison of the deformation of Theory and FEA by gravity μm

Stroke z/mm	Orientation	Analytical	FEA
540	$\theta=0^\circ$	−68.8	−54.8
	$\theta=0^\circ, \psi=0^\circ$	−72.0	−71.6
	$\theta=40^\circ, \psi=90^\circ$	−84.2	−71.9
	$\theta=40^\circ, \psi=180^\circ$	−79.2	−80.9
740	$\theta=0^\circ$	−160.4	−151.3
	$\theta=0^\circ, \psi=0^\circ$	−122.5	−121.1
	$\theta=40^\circ, \psi=90^\circ$	−164.8	−155.1
	$\theta=40^\circ, \psi=180^\circ$	−157.3	−162.3

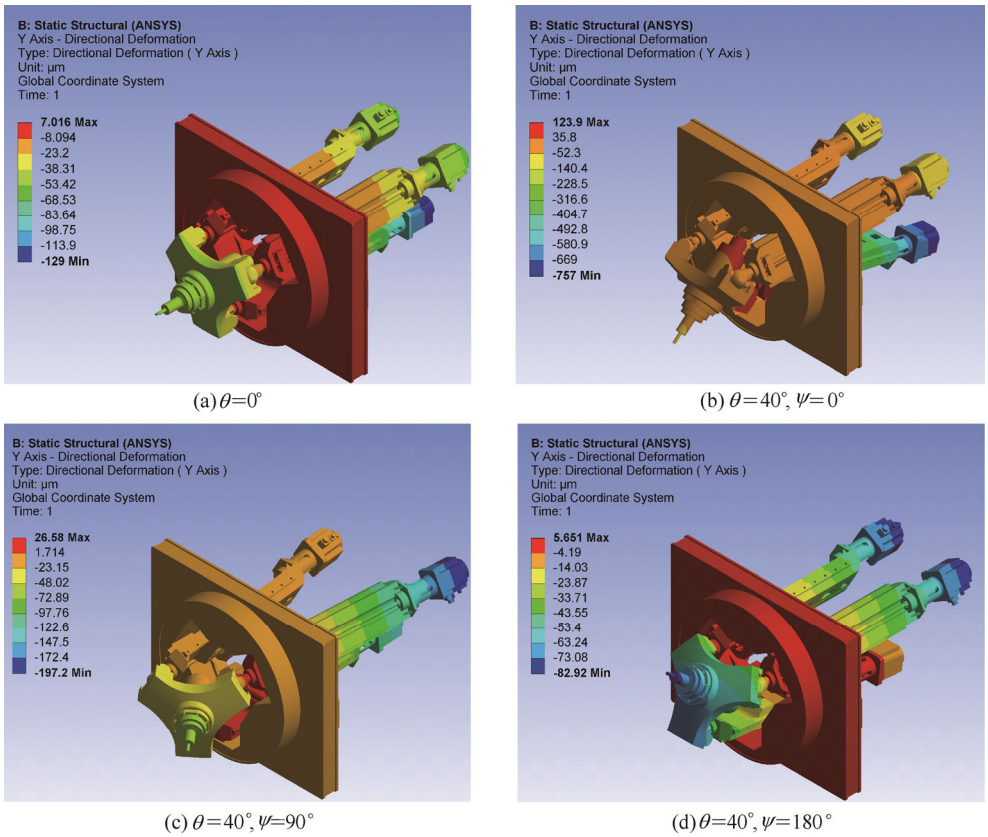

(a) θ=0°　(b) θ=40°, ψ=0°

(c) θ=40°, ψ=90°　(d) θ=40°, ψ=180°

Fig. 12. Deflection of four orientations by gravitational field in z=540 mm

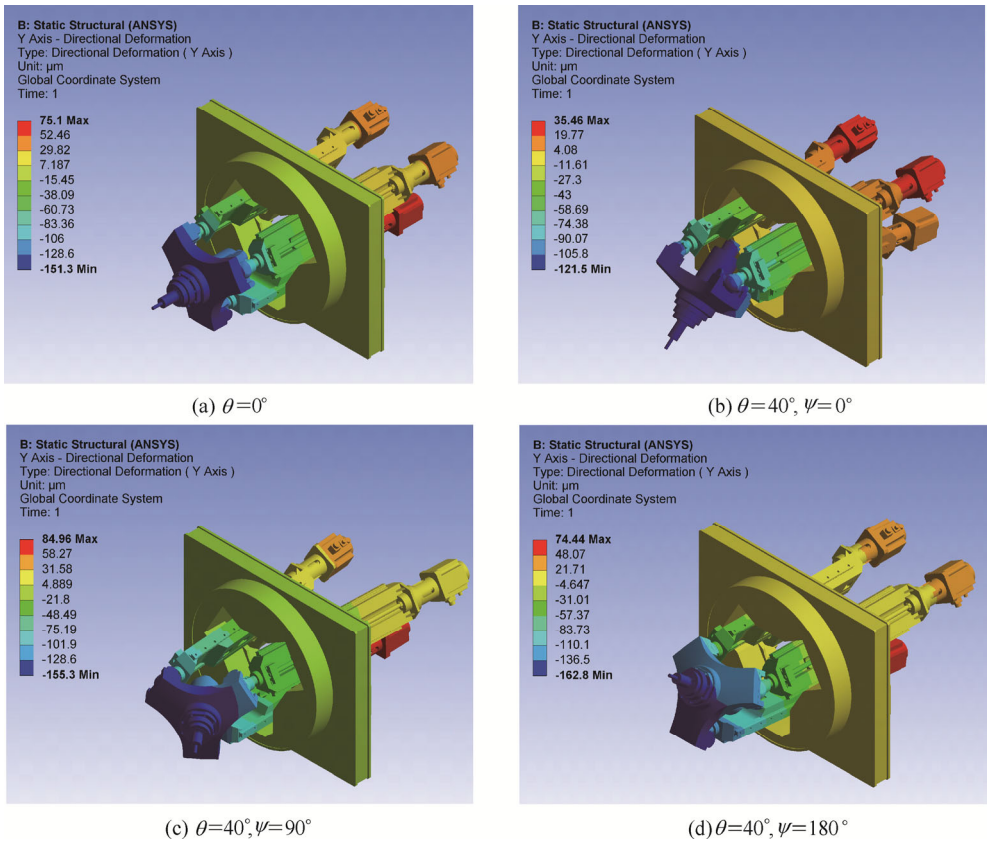

(a) θ=0° (b) θ=40°, ψ=0°

(c) θ=40°, ψ=90° (d) θ=40°, ψ=180°

Fig. 13. Deflection of four orientations by gravitational field in z=740 mm

Meanwhile, the compliance is carried out using experimental method at five configurations(z=540 mm, 590 mm, 640 mm, 690 mm, 740 mm and θ=0°). Fig. 14 shows the experimental set-up where a vertical force is applied by a jack mounted on the spindle flange and its value is read by a force gauge. The deflection at the point where the force is applied is measured by the dial indicator 1. The base deflections are measured by dial indicators 2 and 3 to eliminate the deflection due to compliance of the base. In order to eliminate random errors, the measurements are averaged by ten times. Deflection analysis is also carried out by FEA at the corresponding configurations. Fig. 15 shows the deflections obtained by the semi-analytical method, FEA and experiment. It can be seen that the results obtained by the experiment are slightly higher than the two others.

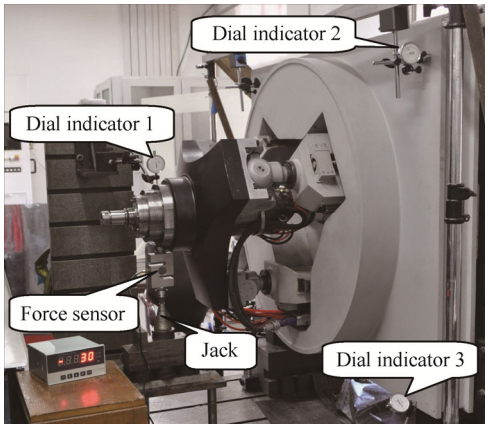

Fig. 14. Compliance measurement experiment

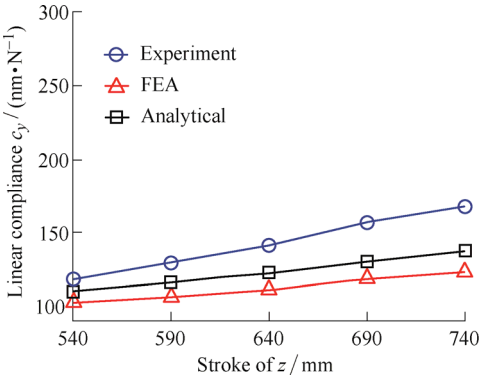

Fig. 15. Results of experiment, FEA and analytical

5 Conclusions

(1) Force analysis shows that the linear map between the externally applied wrench in the operation space and the reaction forces in the joint space is nothing but the overall or generalized Jacobian since the gravity of the moving components can be expressed as an equivalent wrench imposed upon the platform.

(2) The resultant deflection twist of the platform of the A3 head contains two components, i.e. the deflection caused by resultant externally applied wrench, and that transmitted from the joint deflection due to the distributed gravitational forces of the limb-body.

(3) The compliance model of the A3 head allows the distribution of the TCP deflection caused by various components to be evaluated in a very efficient manner as validated by FEA and experiment.

(4) Both computational and experimental results of the A3 head show that the gravity has significant bearing on the pose accuracy. Thus, room remains for the lightweight yet rigidity design of the system as a whole.

References

[1] URIARTE L, ZATARAIN M, AXINTE D, et al, Machine tools for large parts[J]. *CIRP Annals–Manufacturing Technology*, 2013, 62(2): 731–750.

[2] KIM H S, TSAI L W. Design optimization of a Cartesian parallel manipulator[J]. *Journal of Mechanical Design*, 2003, 125(1): 43–51.

[3] HENNES N. Ecospeed: an innovative machining concept for high performance 5-axis-machining of large structural component in aircraft engineering[C]//*Proceedings of the 3rd Chemnitz Parallel kinematics Seminar*, Chemnitz, Germany, 2002: 763–774.

[4] HENNES N, STAIMER D. Application of PKM in aerospace manufacturing high performance machining centers ECOSPEED, ECOSPEED-F and ECOLINER[C]//*Proceedings of the 4th Chemnitz Parallel Kinematics Seminar*, Chemnitz, Germany, 2004: 557–577.

[5] PIRAS G, CLEGHORN W L, MILLS J K. Dynamic finite element analysis of a planar high speed parallel manipulator with flexible links[J]. *Mechanism and Machine Theory*, 2005, 40(7): 849–862.

[6] EL-KHASAWNEH B S, FERREIRA P M. Computation of stiffness and stiffness bounds for parallel link manipulators[J]. *International Journal of Machine Tools and Manufacture*, 1999, 39(2): 321–342.

[7] RIZK R, FAUROUX J C, MUMTEANU M, et al. A comparative stiffness analysis of a reconfigurable parallel machine with three or four degrees of mobility[J]. *Journal of Machine Engineering*, 2006, 6(2): 45–55.

[8] ZHANG J, ZHAO Y Q, DAI J S H. Compliance modeling and analysis of a 3-RPS parallel kinematic machine module[J]. *Chinese Journal of Mechanical Engineering*, 2014, 27(4): 703–713.

[9] HUANG T, ZHAO X Y, WHITEHOUSE D J. Stiffness estimation of a Tripod-based parallel kinematic machine[J]. *IEEE Transactions on Robotics and Automation*, 2002, 18(1): 50–58.

[10] WANG Y Y, LIU H T, HUANG T, et al. Stiffness modeling of the Tricept robot using the overall Jacobian matrix[J]. *ASME Journal of Mechanisms and Robotics*, 2009, 021002.1–021002.8.

[11] GOSSELIN C. Stiffness mapping for parallel manipulator[J]. *IEEE Transactions on Robotics and Automation*, 1990, 6(3): 377–382.

[12] GOSSELIN C, ZHANG D. Stiffness analysis of parallel mechanisms using a lumped model[J]. *International Journal of Robotics and Automation*, 2002, 17(1): 17–27.

[13] BI Z M, LANG S Y T, ZHANG D. Stiffness analysis of a Tripod with a passive link[C]//*Proceedings of International Mechanical Engineering Congress and Exposition*, Florida, USA, November 5–11, 2005: 1665–1671.

[14] ZHANG D, BI Z M, LI B Z. Design and kinetostatic analysis of a new parallel manipulator[J]. *Robotics and Computer-Integrated Manufacturing*, 2009, 25(4–5): 782–791.

[15] PASHKEVICH A, CHABLAT D, WENGER P. Stiffness analysis of over-constrained parallel manipulators[J]. *Mechanism and Machine Theory*, 2009, 44(5): 966–982.

[16] PASHKEVICH A, KLIMCHIK A, CHABLAT D. Enhanced stiffness modeling of manipulators with passive joints[J]. *Mechanism and Machine Theory*, 2011, 46(5): 662–679.

[17] KLIMCHIK A, PASHKEVICH A, CARO S, et al. Stiffness matrix of manipulators with passive joints: computational aspects[J]. *IEEE Transactions on Robotics*, 2012, 28(4): 955–958.

[18] KLIMCHIK A, CHABLAT D, PASHKEVICH A. Stiffness modeling for perfect and non-perfect parallel manipulators under internal and external loadings[J]. *Mechanism and Machine Theory*, 2014, 79(5): 1–28.

[19] REZAEI A, AKBARZADEH A, ENFERADI J. Stiffness analysis of a spatial parallel mechanism with flexible moving platform[C]// *Proceedings of the ASME 10th Biennial Conference on Engineering Systems Design and Analysis*, Istanbul, Turkey, July 12–14, 2010: 647–655.

[20] REZAEI A, AKBARZADEH A, AKBARZADEH-T M-R. An investigation on stiffness of a 3-PSP spatial parallel mechanism with flexible moving platform using invariant form[J]. *Mechanism and Machine Theory*, 2012, 51: 195–216.

[21] LI M, WU H P, HANDROOS H. Static stiffness modeling of a novel hybrid redundant robot machine[J]. *Fusion Engineering and Design*, 2011, 86(9–11): 1838–1842.

[22] YOE S H, YANG G, LIM W B. Design and analysis of cable-driven manipulators with variable stiffness[J]. *Mechanism and Machine Theory*, 2013, 69: 230–244.

[23] LU Y, CHEN L W, WANG P, et al. Statics and stiffness analysis of a novel six-component force/torque sensor with 3-RPPS compliant parallel structure[J]. *Mechanism and Machine Theory*, 2013, 62: 99–111.

[24] WANG D, FAN R, CHEN W Y. Performance enhancement of a three-degree-of-freedom parallel tool head via actuation redundancy[J]. *Mechanism and Machine Theory*, 2014, 71: 142–162.

[25] WANG Y Y, LIU H T, HUANG T, et al. Stiffness modeling of the tricept robot using the overall jacobian matrix[J]. *Journal of Mechanisms and Robotics*, 2009, 1(2): 021002-1-8.

[26] WANG Y Y, HUANG T, ZHAO X M, et al. A semi-analytical approach for stiffness modeling of PKM by considering compliance of machine frame with complex geometry[J]. *Chinese Science Bullentin*, 2008, 53(16): 2565–2574.

[27] KLIMCHIK A, CHABLAT D, PASHKEVICH A. CAD-based approach for identification of elasto-static parameters of robotic manipulators[J]. *Finite Element in Analysis and Design*, 2013, 75: 19–30.

[28] ZHAO T S, ZHAOY Z, BIAN H, et al. Continuous stiffness nonlinear mapping of spatial parallel mechanism[J]. *Chinese Journal of Mechanical Engineering*, 2008, 44(8): 20–32. (in Chinese)

[29] QUENNOUELLE C, GOSSELIN C. Stiffness matrix of compliant parallel mechanisms[C]//*Proceedings of the ASME Mechanisms and Robotics Conference*, New York, USA, August 3–6, 2008: 151–161.

[30] QUENNOUELLE C, GOSSELIN C. Kinematostatic modeling of compliant parallel mechanisms-Application to a 3-PRRR Mechanism, the Tripteron[J]. *Meccanica*, 2011, 46(1): 155–169.

[31] LI Y G, LIU H T, ZHAO X M, et al. Design of a 3-DOF PKM module for large structural component machining[J]. *Mechanism and Machine Theory*, 2010, 45(6): 941–954.

Biographical notes

LI Qi, born in 1984, is currently a PhD candidate at *Key Lab of Mechanism Theory and Equipment Design of Ministry of Education, Tianjin University, China.* His research interests include mechanisms and robotics.
E-mail: liqi@tju.edu.cn

WANG Manxin, born in 1987, is currently a PhD candidate at *Key Lab of Mechanism Theory and Equipment Design of Ministry of Education, Tianjin University, China.* His research interests include mechanisms and robotics
E-mail: wangmxtju@aliyun.com

HUANG Tian, born in 1953, is currently a professor and a PhD candidate supervisor at *Key Lab of Mechanism Theory and Equipment Design of Ministry of Education, Tianjin University, China.* His research interests include mechanisms and robotics.
E-mail: tianhuang@tju.edu.cn

CHETWYND G Derek, born in 1948, is currently a full professor at *School of Engineering, University of Warwick, UK.* His research interests include Precision Engineering and Nanotechnology.
E-mail: D.G.Chetwynd@warwick.ac.uk